DR2004096

DATA REPOSITORY ITEMS

DETAILS OF INCORPORATION OF EARTHQUAKES IN THE MODELING AND OF THE INVERSION FOR THE 2-D S-WAVE VELOCITY STRUCTURE

The nine earthquakes (Fig. 2) were initially located with the whole INDEPTH III array by using a one-dimensional procedure (Lee and Valdés, 1985) and a one-dimensional average velocity model based on the two-dimensional P-wave velocity model (Zhao et al., 2001). The earthquakes were finally incorporated into the two-dimensional model (Zhao et al., 2001). As part of this step, the origin times were adjusted to provide a least-squares best fit to the P-wave traveltimes. Adjustment of the depths was also tried, but this gave poorer results in the two-dimensional inversion for the S-wave velocity structure. Final P- and S-wave record sections for the earthquakes were then plotted. The S-wave traveltime picks from the final record sections formed the basis for the determination of the two-dimensional S-wave velocity model.

The 2-D S-wave velocity model was derived by holding the interfaces from the 2-D P-wave velocity model (Zhao et al., 2001) fixed and then inverting for the S-wave velocities only (Lutter et al., 1990; Zelt and Smith, 1992). 216 travel-time readings from the Sg phase recorded from all of the nine earthquakes and four of the 12 shots were used to invert for the S-wave velocity structure of the top two layers beneath the INDEPTH III profile. The starting model for the inversion had a Vp/Vs ratio for the top layer of 1.90. For the second top layer the starting model had velocities of 3.3-3.4 km/s along the top and 3.4-3.5 km/s along the base. Further, in the second top layer the

vertical velocity gradient in the starting model was chosen such that the Sg rays from

the four northernmost events "newq_1"-"newq_4", penetrating to the base of this layer

would emerge at the surface at about 230 km epicentral distance (Fig. 3A). Beyond this

distance no Sg arrivals were picked and other starting models with smaller gradients

produced Sg travel times which are well in advance of any S-wave energy which can be

recognized in the record sections at epicentral distances in excess of 300 km. As all but

one of the few rays which penetrate the top layer only, emerge at the surface between

model kms 170 and 250, the top layer was modelled with just one independent velocity

parameter. The second top layer was modelled with five independent velocity

parameters. In the inversion, the vertical velocity gradients in both layers were held

fixed. This resulted in the fact that in all iterations of the inversion, the Sg rays from the

four events "newq_1"-"newq_4" penetrating to the base of the second top layer

emerged at the surface at about 230 km epicentral distance. After three iterations the

average absolute travel-time residual between the observed and theoretical onsets had

reduced from 0.92 s (χ^2 = 5.34) in the starting model to 0.47 s (χ^2 = 1.39), with no

further significant improvement occurring. Other starting models with e.g. a constant

Vp/Vs ratio or a laterally homogenous S-wave velocity for the 2nd top layer produced

very similar end models to the one shown here. The normalized travel-time error, χ^2 of

1.39 obtained for the final upper crustal model indicates that the observed data are

appropriately fitted. A χ^2 value of 1.0 indicates an optimum fit between the observed

and calculated travel times but values somewhat greater than 1.0 are also appropriate

especially when the experiment geometry deviates from a straight line and the

modelling approach does not take into account out of plane (3-D) effects (Zelt and

Smith, 1992).

Evidence for low Poisson's ratios in the second layer is present in the data e.g., in the record section for the event "newq_2" (Fig. 3A), Sg arrivals are conspicuously earlier than they would be if Poisson's ratio in the second layer were uniformly around 0.25. Also, the average slope in the Wadati diagram for each of the earthquakes is always less than 0.72, and, as nearly all the arrivals used to determine this slope are Pg arrivals and their corresponding Sg arrivals traveling mainly through the second layer, this average slope is also a good indication that the Poisson's ratio in the second layer is less than 0.25.

38 arrivals from the S-wave phase, SmS, reflected from the Moho were picked from the four events "newq_1"-"newq_4". The SmS observations are around 3 s late with respect to a model in which the middle and lower crust has an average Poisson's ratio of 0.25. The starting model for the inversion was one in which the Vp/Vs ratio for the middle and lower crust was 1.85 (Poisson's ratio of 0.29). Only one independent velocity parameter was inverted for. The one iteration which was necessary to achieve convergence reduced the average absolute travel-time difference between the observed and theoretical arrivals from 0.69 s (^{2} = 1.98) to 0.63 s (^{2} = 1.64) and resulted in a velocity increase of 0.02 km/s. Again the ^{2} value of 1.64 for the final middle and lower crustal model indicates that the observed data are quite appropriately fitted. The reason for the such small improvement between the start and final models is that the start model was chosen to be fairly close to the final model. This was done in order to ensure that the final model was also essentially a constant Poisson's ratio model although the updated values in the inversion were S-wave velocities.

The model with a constant Poisson's ratio for the middle and lower crust is thought to be one of the simplest models that can be derived and is probably all that can be justified with the available data. However, one advantage of the model is that the middle crust and the upper part of the lower crust define a low-velocity zone with respect to the upper crust. This low-velocity zone ensures that there are no theoretical S-wave arrivals that are too early with respect to observed S-wave energy at epicentral distances beyond 250 km (see Fig. 3A).

In order to prevent theoretical onsets from the refracted phase, Sn, through the uppermost mantle from arriving earlier than any observed S-wave energy on the record sections at epicentral distances around 300 km, the S-wave velocity in the uppermost mantle was assigned values of 4.5–4.6 km/s. This resulted in a Poisson's ratio for the uppermost mantle of 0.27.

DETAILS OF GEOLOGICAL REQUIREMENTS

Geological maps and tectonic models (Fig. DR3A-B) indicate that the INDEPTH III region of central Tibet is underlain by quartz-rich upper and middle crust and that the - quartz transition (ABQT) does not likely coincide with a major lithological or structural boundary within the Tibetan crust. The maps and cross-sections emphasize the spatial variability in upper crustal shortening (e.g. Yin and Harrison, 2000; Tapponnier et al., 2001), but highlight the uncertainties how the middle and lower crust of Tibet accommodated upper crustal shortening. The upper panel of Figure DR3B offers our preferred scenario that in essence corresponds to a section across western

Tibet by Kapp et al. (2003). The structure of the Lhasa (Amdo anticlinorium) and Qiangtang (Shuang Hu anticlinorium) blocks results from Early Cretaceous-Tertiary northward underthrusting of the Lhasa block beneath the Qiangtang block along the Bangong-Nujiang suture. In this interpretation the upper and middle crust of central Tibet is composed of cover and basement of the Lhasa block. Lhasa block cover is carbonatic-siliciclastic (e.g. Yin et al., 1988), while the basement comprises granitoids, their gneissose equivalents and high-grade metamorphic rocks, all quartz-rich (e.g., Xu et al., 1985; Fraser et al., 2001). The lower panel suggests Cretaceous northward underthrusting of the Lhasa block underneath the Qiangtang block, followed by Tertiary underthrusting of the Qiangtang block underneath the Lhasa block (cf. Tapponnier et al., 2001). The Lhasa and Qiangtang blocks were likely contiguous up to the late Paleozoic, but the characteristic rock assemblage of the Qiangtang block is metasedimentary and metavolcanic melange including felsic gneiss, originating from early Mesozoic southward subduction of the Songpan-Ganze siliciclastic flysch of northern Tibet along the Jinsha suture. The melange was exhumed to shallow and mid crustal levels already during the early Mesozoic (cf. Kapp et al., 2000). Irrespective of the tectonic model adopted, (1) the region of the Bangong-Nujiang suture is underlain by quartz-rich crust of the Lhasa and Qiangtang blocks that have likely an identical basement and a quartz-rich cover, (2) the inferred position of the ABQT cuts across the interpreted structural boundaries at least in large parts of the sections.

Muscovite-bearing, quartz-rich felsic rocks should contain a few percent of partial melt at the ABQT. However, as felsic melt at low degrees of partial melting does not form interconnected films at grain boundaries, the effect on seismic velocities and electrical

conductivity is relatively small and the effect on the predicted P- and S-wave velocity and density changes at the ABQT is negligible. In the case of spherical inclusions of the liquid phase, 2% of melt will cause some 2% drop in both the P- and S-wave velocities, which is hardly detectable with the wide-angle seismic reflection or refraction method. In the more probable case of more dry, biotite-bearing felsic rocks in the Tibetan crust (Hacker et al., 2000), the solidus is shifted to about 800 °C and significant melting should not occur until some kilometers below the ABQT.

REFERENCES CITED

Fraser, J.E., Searle, M.P., Parrish, R.R. and Noble, St.R., 2001, Chronology of deformation, metamorphism, and magmatism in the southern Karakoram Mountains: Geological Society of America Bulletin, v. 113, p. 1443-1455.

Hacker, B.R., Gnos, E., Ratschbacher, L., Grove, M., McWilliams, M., Sobolev, S.V., Wan, J., and Zhenhan, W., 2000, Hot and dry deep crustal xenoliths from Tibet: Science, v. 287, p. 2463–2466.

Kapp, P., Yin, A., Manning, C.E., Murphy, M., Harrison, T.M., Spurlin, M., Lin, D., Xi-Guang, D. and Cun-Ming, W., 2000, Blueschist-bearing metamorphic core complexes in the Qiangtang block reveal deep crustal structure of northern Tibet: Geology, v. 28, p. 19-22.

Kapp, P., Murphy, M.A., Yin, A., Harrison, T.M., Ding, L. and Guo, J., 2003, Mesozoic and Cenozoic tectonic evolution of the Shiquanhe area of western Tibet, Tectonics, v. 22, 1029, doi:10.1029/2001TC001332.

Lee, W.H.K., and Valdés, C.M., 1985, HYPO71PC: A personal computer version of the HYPO71 earthquake location program: U.S. Geological Survey Open-File Report 85-749, 43 p.

Liu, Z.Q.C., 1988, Geologic Map of the Qinghai-Xizang Plateau and its Neighboring Regions: Geological Publishing House, Beijing, scale 1:1,500,000.

Lutter, W.J., Nowack, R.L. and Braile, L.W., 1990, Seismic imaging of upper crustal structure using travel times from the PASSCAL Ouachita experiment: Journal of Geophysical Research, v. 95, p. 4621-4631.

Tapponnier, P., Zhiqin, X., Roger, F., Meyer, B., Arnaud, N., Wittlinger, G. and Jingsui, Y., 2001, Oblique stepwise rise and growth of the Tibet plateau: Science, v. 294, p. 1671-1677.

Xu, R.-H., Schärer, U. and Allégre, C.J., 1985, Magmatism and metamorphism in the Lhasa block (Tibet): a geochronological study: Journal of Geology, v. 93, p. 41-57.

Yin, A. and Harrison, T.M., 2000, Geologic evolution of the Himalayan-Tibetan orogen: Annual Review of Earth and Planetary Sciences, v. 28, p. 211-280.

Yin, J., Xu, J., Liu, C. and Li, H., 1988, The Tibetan plateau: regional stratigraphic context and previous work: Royal Society of London Philosophical Transactions, ser. A, v. 327, p. 5-52.

Zelt, C.A. and Smith, R.B., 1992, Seismic traveltime inversion for 2-D crustal velocity structure: Geophysical Journal International, v. 108, p. 16-34.

Zhao, W., Mechie, J., Brown, L.D., Guo, J., Haines, S., Hearn, T., Klemperer, S.L., Ma, Y.S., Meissner, R., Nelson, K.D., Ni, J.F., Pananont, P., Rapine, R., Ross, A. and Saul, J., 2001, Crustal structure of central Tibet as derived from project INDEPTH wide-angle seismic data: Geophysical Journal International, v. 145, p. 486-498.
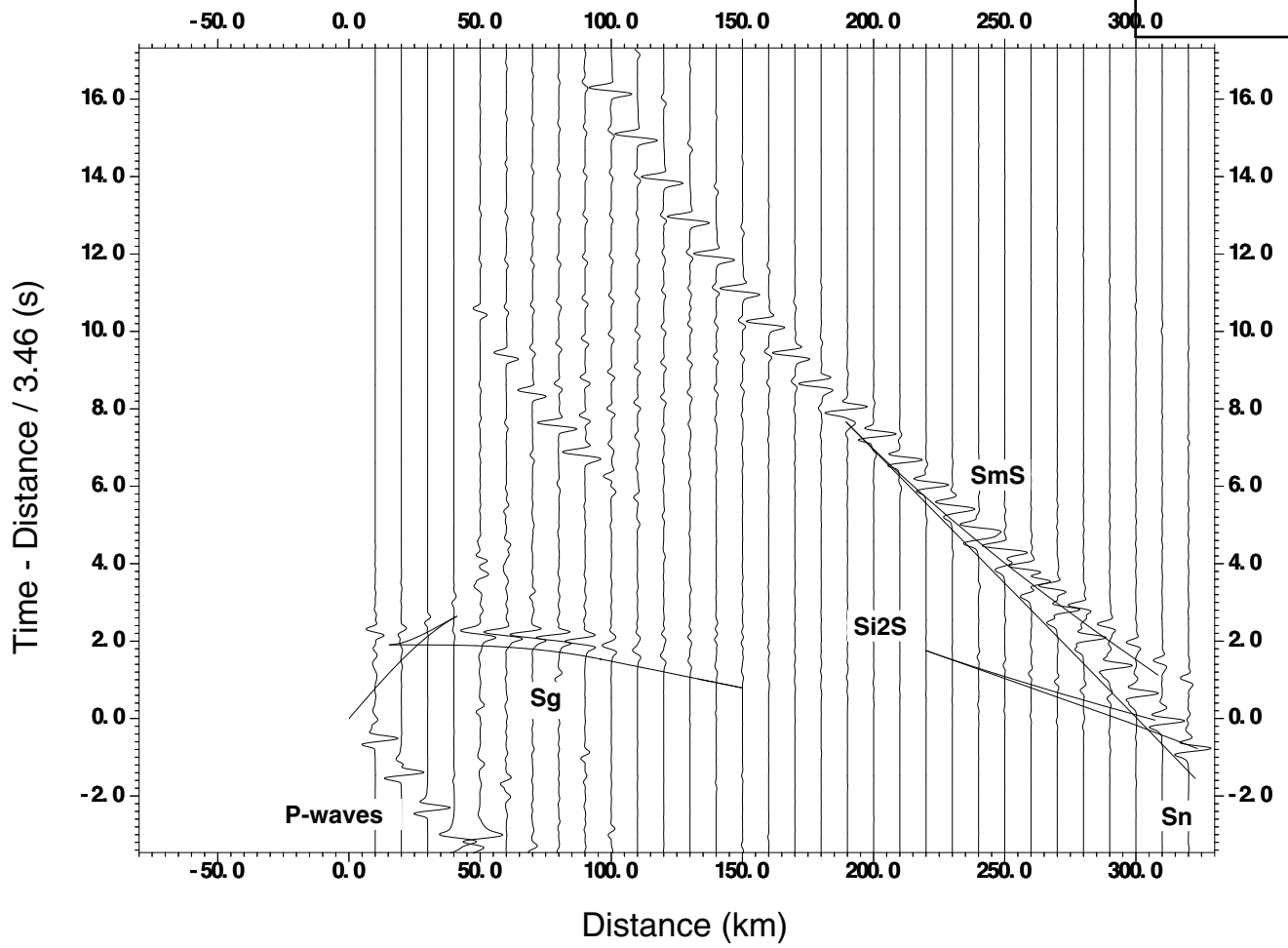
Figure Captions

Fig. DR1. Synthetic seismograms calculated using the reflectivity method for the model shown in Fig. 1A. The record section reduced with a velocity of 3.46 km/s shows the radial component of S-wave motion in which each trace is normalized individually. The seismograms have been calculated for a dominant frequency of 2 Hz which is approximately the dominant frequency in the wide-angle earthquake data shown in Fig. 3A. Continuous lines represent phases calculated from the model in Fig. 1A. Key: Sg - refraction through the upper crust; Si2S - reflection from the top of the lower crust; SmS - reflection from the Moho, Sn - refraction through the uppermost mantle. Note the absence of a reflection from the   -   quartz transition (ABQT).
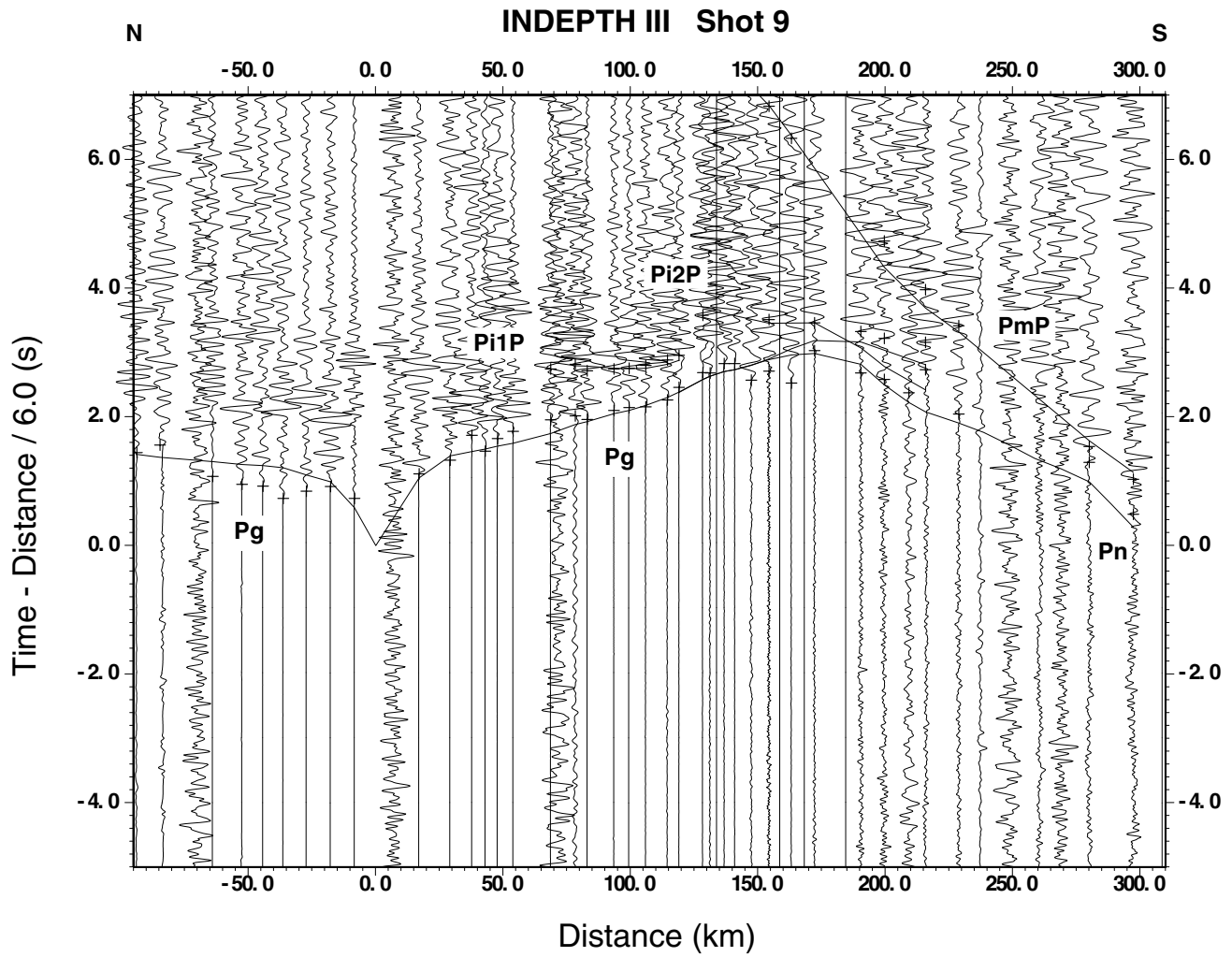
Fig. DR2. Seismic data from shot 9 recorded along the INDEPTH III NNW-SSE profile. The record section reduced with a velocity of 6 km/s shows the vertical component of P-wave motion in which each trace is normalized individually and bandpass filtered from 2 to 12 Hz. Continuous lines represent phases calculated from the 2-D P-wave velocity model (Fig. 4) (Zhao et al., 2001) while crosses represent travel-time picks. Note that the shot data have a dominant frequency of around 7-8 Hz in contrast to the dominant frequency of around 2 Hz for the earthquakes. Note also that although the Pi1P phase can be observed over a similar epicentral distance range as in the synthetic data (60 km in the observed data versus 80 km in the synthetic data), it occurs at slightly smaller epicentral distances in the observed data than in the synthetic data (65-125 km epicentral distance in the observed data versus 90-170 km epicentral distance in the synthetic data). This is due to the fact that the velocity structure differs in

that part of the 2-D model (Zhao et al., 2001) through which the rays from shot 9 pass, from the average velocity structure of the synthetic model. Key: Pg - first arrival refraction through the upper crust; Pi1P - reflection from the ABQT (top of the middle crust); Pi2P - reflection from the top of the lower crust; PmP - reflection from the Moho; Pn - first arrival refraction through the uppermost mantle.
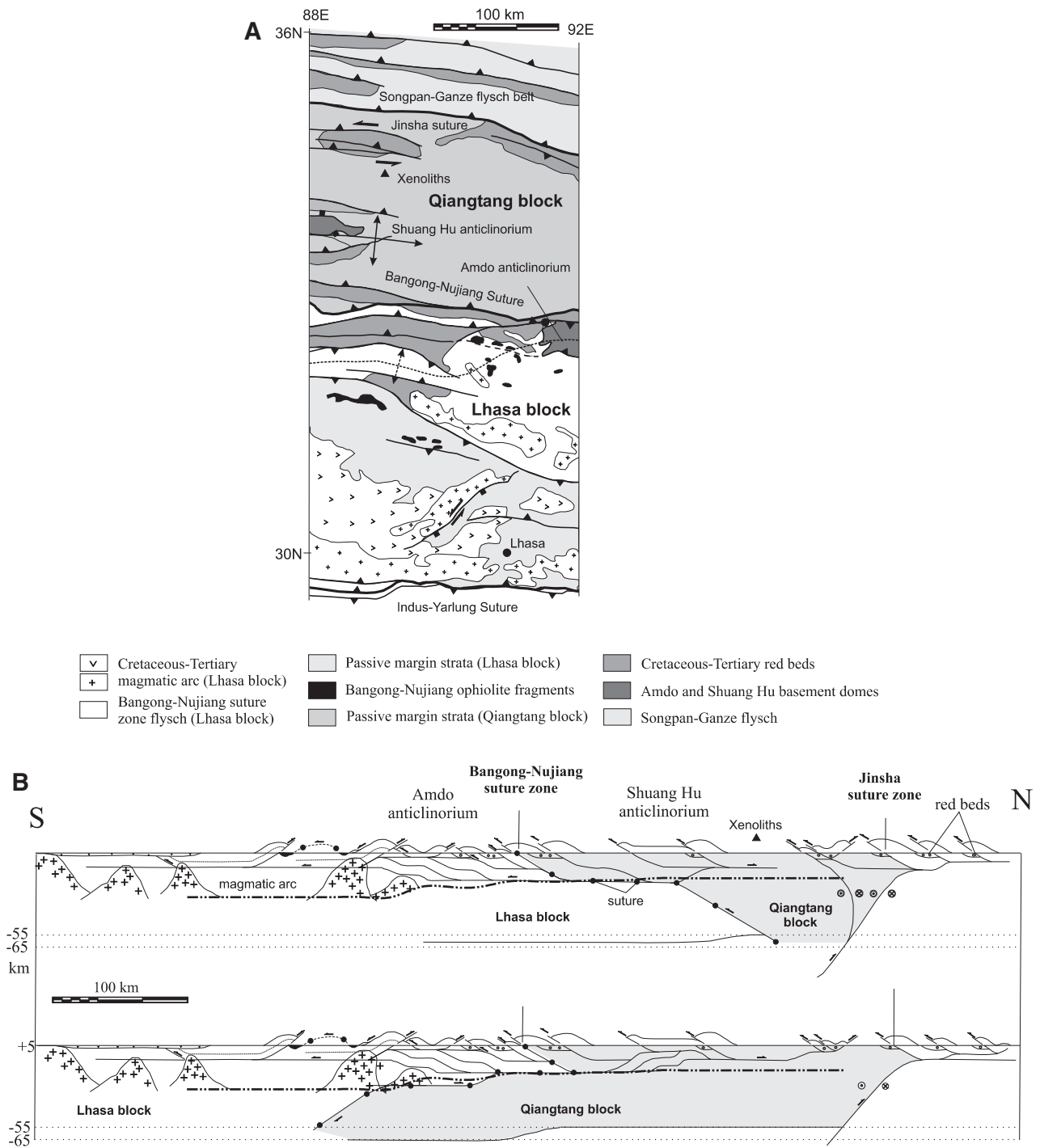
Fig. DR3. A) Strip map covering the area between the Indus-Yarlung suture zone in the S and the Songpan-Ganze flysch belt in the N, integrating surface geologic data in the east-central part of the plateau and highlighting Late Mesozoic-Cenozoic structures. Map and schematic cross-sections in B) are based on interpretations of mapping at scales of 1:1,500,000 (Liu, 1988) and INDEPTH field studies. B) Upper crustal thickening structures and two solutions for their middle-lower crustal accommodation. In the upper panel, the entire thrust belt of the Lhasa (Amdo anticlinorium) and southern Qiangtang (Shuang Hu anticlinorium) blocks formed by long-lived northward underthrusting of the Lhasa block beneath the Qiangtang block. The lower panel suggests that initial (Cretaceous) northward underthrusting of the Lhasa block underneath the Qiangtang block was followed by Tertiary underthrusting of the Qiangtang block underneath the Lhasa block.

Mechie_Fig. DR1

Mechie_Fig. DR2

A

88E   100 km
36N   92E

Songpan-Ganze flysch belt

Jinsha suture

Xenoliths

Qiangtang block

Shuang Hu anticlinorium

Amdo anticlinorium

Bangong-Nujiang Suture

Lhasa block

Lhasa

30N

Indus-Yarlung Suture

Cretaceous-Tertiary magmatic arc (Lhasa block)	Passive margin strata (Lhasa block)	Cretaceous-Tertiary red beds
	Bangong-Nujiang ophiolite fragments	Amdo and Shuang Hu basement domes
Bangong-Nujiang suture zone flysch (Lhasa block)	Passive margin strata (Qiangtang block)	Songpan-Ganze flysch

B

S

Amdo anticlinorium

Bangong-Nujiang suture zone

Shuang Hu anticlinorium

Jinsha suture zone

red beds   N

Xenoliths

magmatic arc

Lhasa block

suture

Qiangtang block

-55
-65
km

100 km

+5

Lhasa block

Qiangtang block

-55
-65

Mechie_Fig. DR3